Geochemistry Geophysics Geosystems G3

Article
Volume 11, Number 6
4 June 2010
Q06004, doi:10.1029/2010GC003038
ISSN: 1525-2027

Published by AGU and the Geochemical Society

Constraints on upper mantle viscosity from the flow-induced pressure gradient across the Australian continental keel

Christopher Harig

Department of Geological Sciences, University of Colorado at Boulder, Benson Earth Sciences Building, Boulder, Colorado 80309, USA (harig@colorado.edu)

Also at Cooperative Institute for Research in Environmental Science, University of Colorado at Boulder, Boulder, Colorado 80309, USA

Shijie Zhong

Department of Physics, University of Colorado at Boulder, Duane Physics Building, Boulder, Colorado 80309, USA (szhong@colorado.edu)

Frederik J. Simons

Department of Geosciences, Princeton University, Guyot Hall, Princeton, New Jersey 08544, USA (fjsimons@alum.mit.edu)

[1] The thickness of continental lithosphere varies considerably from tectonically active to cratonic regions, where it can be as thick as 250–300 km. Embedded in the upper mantle like a ship, when driven to move by a velocity imposed at the surface, a continental keel is expected to induce a pressure gradient in the mantle. We hypothesize that the viscosity of the asthenosphere or the shear coupling between lower lithosphere and asthenosphere should control this pressure effect and thus the resulting dynamic topography. We perform three-dimensional finite element calculations to examine the effects of forcing a continental keel by an imposed surface velocity, with the Australian region as a case study. When the upper mantle is strong but still weaker than the lower mantle, positive dynamic topography is created around the leading edge, and negative dynamic topography is created around the trailing edge of the keel, which is measurable by positive and negative geoid anomalies, respectively. For a weak upper mantle the effect is much reduced. We analyze geoidal and gravity anomalies in the Australian region by spatiospectral localization using Slepian functions. The method allows us to remove a best fit estimate of the geographically localized low spherical harmonic degree contributions. Regional geoid anomalies thus filtered are on the order of ±10 m across the Australian continent, with a spatial pattern similar to that predicted by the models. The comparison of modeled and observed geoid anomalies places constraints on mantle viscosity structure. Models with a two-layer mantle cannot sufficiently constrain the ratio of viscosity between the upper and lower mantle. The addition of a third, weak, upper mantle layer, an asthenosphere, amplifies the effects of keels. Our three-layer models, with lower mantle viscosity of 3×10^{22} Pa s, suggest that the upper mantle (asthenosphere) is 300 times weaker than the lower mantle, while the transition zone (400–670 km depths) has a viscosity varying between 10^{21} and 10^{22} Pa s.

Components: 13,900 words, 7 figures.

Keywords: asthenosphere; mantle; rheology; continental keel; geoid; spatiospectral localization.

Index Terms: 8122 Tectonophysics: Dynamics: gravity and tectonics (8033); 8162 Tectonophysics: Rheology: mantle (8033); 8103 Tectonophysics: Continental cratons.

Received 11 January 2010; **Revised** 1 April 2010; **Accepted** 7 April 2010; **Published** 4 June 2010.

Harig, C., S. Zhong, and F. J. Simons (2010), Constraints on upper mantle viscosity from the flow-induced pressure gradient across the Australian continental keel, *Geochem. Geophys. Geosyst.*, *11*, Q06004, doi:10.1029/2010GC003038.

1. Introduction

[2] Our understanding of Earth's deformation and dynamics fundamentally depends on the rheology of the mantle. The viscosity structure of the mantle has been inferred mainly by studying the response to disappearing glacial surface loads over the past 10^5 years [e.g., *Cathles*, 1975; *Peltier*, 1976; *Wu and Peltier*, 1983; *Yuen and Sabadini*, 1985; *Nakada and Lambeck*, 1989; *Lambeck et al.*, 1990; *Mitrovica*, 1996; *Simons and Hager*, 1997; *Mitrovica et al.*, 2007] and by examining geophysical signals from models of mantle convection, such as long-wavelength geoid anomalies and surface plate velocities [e.g., *Hager*, 1984; *Ricard et al.*, 1984; *Hager and Richards*, 1989; *King and Masters*, 1992; *Forte and Peltier*, 1994]. Results from these methods have not always been consistent. Analyses of convection-related observables have routinely suggested that the upper mantle is less viscous than the lower mantle by a factor of at least 30, and perhaps as much as 300. On the other hand, studies of glacial isostatic adjustment sometimes argue for less than a factor of 10 variation [*Peltier*, 1998]. Jointly inverting several types of data has provided additional detail [e.g., *Mitrovica and Forte*, 2004], but the mantle's viscosity structure remains incompletely resolved. This is mainly due to the poor vertical resolution of the postglacial rebound data [*Paulson et al.*, 2007a, 2007b]. Here, we consider whether pressure gradients across continental keels can be used to place a meaningful constraint on the viscosity of the upper mantle.

[3] The thickness of the continental lithosphere varies considerably from tectonically active to stable cratonic regions [*Artemieva*, 2009]. Determining the depths of continental keels has been an area of much study and debate over the past several decades [*King*, 2005], with estimates historically ranging from 175 to 400 km. Observations of surface heat flux, for example, suggest a thick Archean lithosphere [e.g., *Rudnick et al.*, 1998], though nowhere exceeding 250 km [e.g., *Ballard and Pollack*, 1987; *Nyblade and Pollack*, 1993; *Jaupart et al.*, 1998]. Analyses of mantle xenoliths, if indeed representative of a conductive geotherm, have led to thickness estimates in the lower end of the range, 150–200 km [*Rudnick et al.*, 1998]. Measurements of electrical conductivity show that differences between oceanic and Archean cratonic regions are limited to depths shallower than 250 km [*Hirth et al.*, 2000]. Seismically, lithosphere is typically considered to extend to depths where shear wave speeds are significantly faster than the global average speed (usually >1.5%–2%) [*Masters et al.*, 1996; *Mégnin and Romanowicz*, 2000; *Simons and van der Hilst*, 2002; *Ritsema et al.*, 2004]. While some types of data are known to be influenced by anisotropy in the upper mantle [*Ekström and Dziewoński*, 1998; *Gung et al.*, 2003], most recent seismic estimates generally limit lithospheric thickness to at most 300–350 km [*Artemieva*, 2009]. Overall, across disciplines, the continental keel thickness estimates are in the range of 200–300 km. In particular, Australia, our region of interest, consistently yields some of the highest estimates of any craton, with fast seismic wave speed anomalies persistent to depths of 250–300 km in models of V_{SV}, the vertically polarized shear wave speed [e.g., *Debayle and Kennett*, 2000a; *Simons et al.*, 2002; *Ritsema et al.*, 2004].

[4] The base of the lithosphere has much significance to geodynamics since, as a mechanical lower boundary, it separates the rocks which remain coherent parts of the lithosphere over geologic time from those below that are part of the convecting mantle [*Turcotte and Oxburgh*, 1967]. It is for this reason that such thick continental keels are expected to translate with plate motion over long time scales; an observation that is corroborated by the global correlation of continental crustal age with lithospheric thickness at long wavelengths [*Simons and van der Hilst*, 2002]. Furthermore, continental keels influence the coupling between mantle and lithosphere, thus affecting net rotation of lithosphere [*Zhong*, 2001; *Becker*, 2006, 2008] as well as regional lithospheric deformation [*Conrad and Lithgow-Bertelloni*, 2006].

[5] The motion of continental keels through the upper mantle, which is relatively less viscous, can be expected to induce pressure perturbations in the mantle moving around them [*Ricard et al.*, 1988]. Such pressure gradients will mainly be controlled by the viscosity and thickness of the asthenospheric channel below the lithosphere. If the viscosity of

this channel is low relative to the rest of the mantle the pressure gradient should cause return flow beneath the keel with little effect on dynamic topography at the Earth's surface. However at higher asthenospheric viscosities the return flow should be reduced in favor of a signal in the surface topography and hence gravity anomalies or the geoid. *Ricard et al.* [1988] used an approximate mode-coupling method to estimate these geoidal anomalies in the tens of meters.

[6] In this study we constrain the viscosity of the upper mantle by comparing modeled dynamic geoid anomalies to observations. As these signals are proportional to the magnitude of velocity change across the mantle, we focus on the Australian continent, with its relatively large surface velocities. We analyze the regional geoidal anomalies by spatiospectral localization using Slepian functions. Our results will also be applicable to understanding the development of seismic anisotropy beneath continental cratons and the orientation of the lithospheric stress field surrounding them.

2. Analytical Treatment

[7] To illuminate the physics, we first consider a simplified problem in two dimensions (2-D) that can be solved analytically by neglecting flow in the third dimension, normal to surface motion. We examine the flow at two locations: in the far field, in which a lithosphere of uniform thickness moves over a layered viscosity structure, and the flow beneath a keel, where a much thicker lithosphere moves over the same layers. In both of these locations we would expect only horizontal flow. Therefore, from conservation of mass, the amount of horizontal flow at these locations should balance each other. This takes the form of the flux balance

$$\int_K u(z)dz = \int_F u(z)dz, \tag{1}$$

where the material flux across a vertical plane is the integral of the horizontal velocity function u over depth. Horizontal and vertical coordinates are represented by x and z, and the subscript K indicates the location under the keel, while F indicates the far field (see the notation section). This is also illustrated in the cartoon in Figure 1a, where the

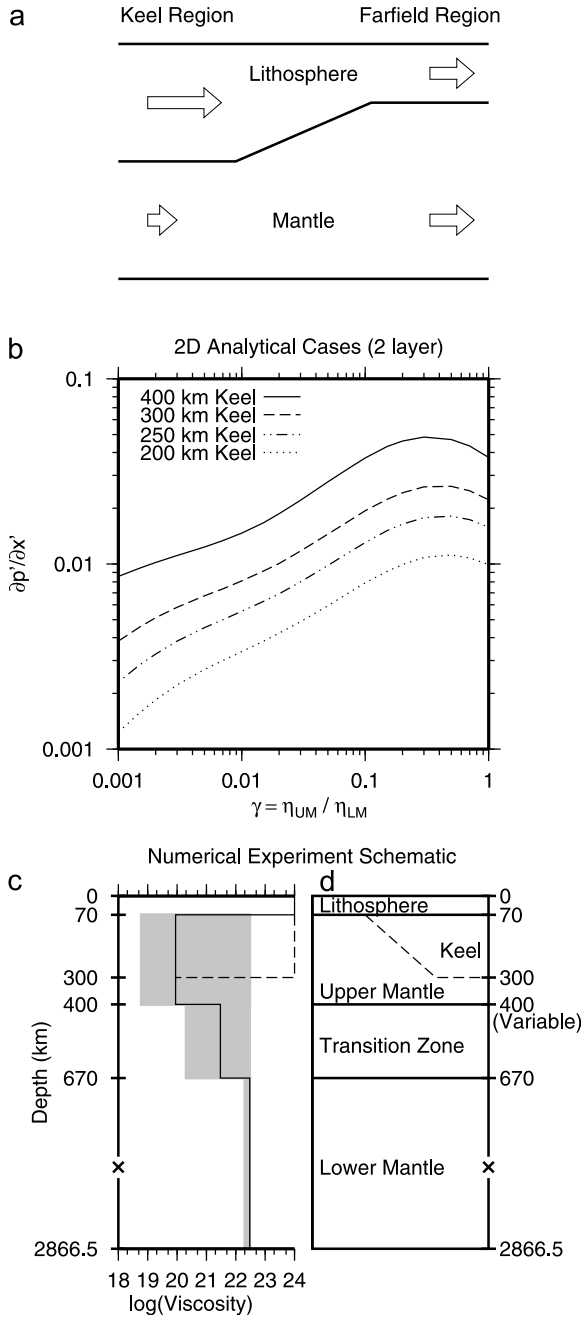

Figure 1. (a) Cartoon illustrating the mass balance argument in the analytical treatment in section 2. Arrows represent the amount of mass transported in each region. Since the lithosphere moves with constant motion, the flow in the mantle must balance the excess mass transported in regions of thick lithosphere (i.e., the keel region). (b) Dimensionless pressure gradients from the two-layer analytical solution (equation (6)) for various keel thicknesses and γ, the ratio of upper mantle to lower mantle viscosities. (c and d) Numerical experiment schematic. Figure 1c shows viscosity variation with depth. Solid line is the preferred model, and dashed line shows keel viscosity. Grey shades show variations of viscosity considered. Figure 1d shows assumed layering. Maximum keel depth is 300 km. Upper mantle–transition zone boundary is varied to set channel thickness between the keel and transition zone.

arrows representing the amount of mass flow change with depth but sum to the same amount in each region. Since the motion of the lithosphere is constant, the flow in the mantle must balance the excess mass transported in regions of thick lithosphere (i.e., keel regions). In one-dimensional channel flow [*Turcotte and Schubert*, 2002], the equation of motion can be written as

$$\frac{\partial \tau}{\partial z} = \frac{\partial p}{\partial x} \quad \text{or} \quad \eta \frac{\partial^2 u}{\partial z^2} = \frac{\partial p}{\partial x}, \tag{2}$$

where τ is the shear stress and p the pressure. The viscosity, η, is assumed to be constant in each layer. By integration we obtain an equation for the velocity, u, as a function of depth, which is subsequently solved for by applying the boundary conditions. These are: constant velocity at the surface, and fixed zero velocity at the bottom. In the far-field case of surface-driven motion, $\partial p/\partial x$ can be considered as zero, and we have linear velocity functions with velocity everywhere in the same direction as the top surface. Underneath the keel, a horizontal pressure gradient is allowed and can be solved for when balancing the material flux.

[8] We simplify our solutions by nondimensionalizing pressure and coordinates by the relevant length, mass, and time scales. For layers with constant viscosity we use

$$p' = \frac{p}{\left(\frac{u_0 \eta_{LM}}{h_0}\right)} \quad \text{and} \quad x' = \frac{x}{h_0}, \tag{3}$$

where p' is dimensionless pressure, x' is dimensionless horizontal coordinate, u_0 is the horizontal velocity at the surface, η_{LM} is the viscosity of the lower mantle, and h_0 is the thickness of the upper mantle in the nonkeel region. Values such as the thickness of the upper mantle channel below the keel, h, and the thickness of the lower mantle, d, nondimensionalize to $h' = h/h_0$ and $d' = d/h_0$. We also use $k = h_0 - h$ as the thickness difference between the keel and the surrounding lithosphere, written dimensionless as $k' = (h_0 - h)/h_0$.

[9] For a uniformly viscous mantle the keel-induced pressure gradient is a well-known result, which varies as the cube of the channel thickness, h, written as

$$\frac{\partial p}{\partial x} = 6 u_0 \eta \frac{k}{h^3} \quad \text{or} \quad \frac{\partial p'}{\partial x'} = 6 \frac{k'}{h'^3}. \tag{4}$$

This is similar to *Turcotte and Schubert* [2002, equation 6-22], except that we allow for a non-zero far-field flux equal to that of uniformly thick lithosphere.

[10] When the mantle has multiple viscous layers, the dependence on the thickness of the weakest layer is more complex. For a two-layered mantle, velocity is solved for in each layer, and then the dimensionless pressure gradient can be written as

$$\frac{\partial p'}{\partial x'} = \frac{\gamma\left(\frac{h'^2 - \gamma d'^2}{\gamma d' + h'}\right) - \gamma\left(\frac{1 - \gamma d'^2}{\gamma d' + 1}\right)}{\frac{1}{2}\left(h'^2 - \gamma d'\right)\left[\frac{\gamma(-2d'h' - d'^2) - h'^2}{\gamma d' + h'}\right] + A}, \tag{5}$$

$$A = -\frac{1}{3}\gamma d'^2 (2d' + 3h') + \frac{h'^3}{3}. \tag{6}$$

Here, $\gamma = \eta_{UM}/\eta_{LM}$ is the ratio of the viscosities of both layers. Setting the thickness of the lower mantle, d', to zero reduces equation (6) to equation (4). Assuming that the thicknesses of the upper and lower mantle are fixed with the boundary at 670 km depth, we plot the pressure gradient versus γ, the ratio of upper mantle to lower mantle viscosities, for several keel thicknesses (Figure 1b). As expected, a thicker continental keel results in larger dimensionless pressure gradients. More interesting, however, is the variation with γ. As γ is decreased from one (uniform viscosity mantle), pressure gradients initially increase even though upper mantle viscosity is lower. Pressure gradients eventually peak, and decrease with decreasing γ.

[11] We also considered a three-layered mantle with a fixed 300 km thick keel and another division around 400 km depth. While this system is more complex, the cases we checked showed a weak upper mantle may result in increased pressure gradients and thus increased dynamic topography, as in the two-layered case.

[12] The analytical model illuminates the problem of flow-generated dynamic topography in the following ways. First, the addition of a weak layer in the upper mantle can enhance the effect of continental keels and increase pressure gradients. Second, the magnitude of surface velocity exerts strong control over dynamic topography since it directly scales the pressure gradient, as per equation (3): the higher the surface velocity, the more dynamic topography can be generated in the system.

[13] While idealized, a 2-D analytical treatment of the problem easily illustrates our hypothesis: that continental keels induce both horizontal variations

in mantle velocity and pressure that are controlled by the details of the viscosity structure. We continue this analysis with more realistic three-dimensional (3-D) calculations, focusing on the unique gravity signals resulting from the dynamic topography. The absence or presence of these signals in Earth's observed gravity field then allow us to bound the plausible viscosity structure below.

3. Numerical Experiment Setup

[14] Our keel models are kept relatively simple, since we intend to examine the first-order effects of their motion only. We begin by assuming boundary-driven flow, and neglect mantle and crustal buoyancy forces. This Stokes flow problem is governed by two of the conservation equations of viscous fluids, those for mass and momentum, represented in dimensionless form as

$$\nabla \cdot \mathbf{v} = 0, \tag{7}$$

$$-\nabla p + \nabla \cdot \left[\eta\left(\nabla \mathbf{v} + \nabla^{\mathrm{T}}\mathbf{v}\right)\right] = 0, \tag{8}$$

where $\mathbf{v}$, p, and η are the velocity vector, pressure, and viscosity, respectively.

[15] These equations are solved with the parallel finite element code CitcomCU [*Moresi and Gurnis*, 1996; *Zhong*, 2006]. We design our model space in regional spherical geometry to span depths from the surface to the core-mantle boundary (CMB), and to cover a 120° by 120° area. Typical resolution for each case is 192, 192, and 104 elements in longitude, latitude, and radial direction, respectively, giving 0.625° per element of horizontal resolution. Vertical resolution is enhanced in the upper mantle at the expense of lower mantle resolution to properly resolve the expected large vertical gradients in horizontal velocity. The upper mantle (between 70 and 670 km depth) has 10 km per element of radial resolution, while the lower mantle and lithosphere above 70 km depth have 57.8 km and 14 km per element of radial resolution, respectively. We specify the thickness of lithosphere at every column of elements and center the keel in our model space at 60° longitude, 0° latitude. The surface velocity is then fixed to result from an Euler pole rotation with an axis at 90° latitude with rotation magnitude of 1 cm/yr. We use a fixed boundary condition on the bottom, which will be discussed further later. On the sides of our box that are parallel to the flow direction we use reflecting boundary conditions. On the sides perpendicular to flow, we use periodic boundary conditions which allow free throughflow with identical velocity on either side. Thus the combined velocity solutions for the side boundaries are mass preserving. Perturbations to the pressure field caused by the keel motion result in dynamic topography at the surface. We analyze the gravity anomalies associated with this dynamic topography and make comparisons to the observed field.

[16] Since dynamic topography directly scales with the magnitude of surface velocity for the Newtonian rheology used in our calculations, we focus our study on the Australian continent, which is the fastest moving continental plate. When imposing surface velocity we use the azimuth of plate motion at the center (130°E, 25°S) of Australia's lithospheric keel from the HS3-NUVEL1A model, which is 1.81° east of north [*Gripp and Gordon*, 2002] and, later, scale the results by the surface velocity magnitude of 8.267 cm/yr. The prescribed surface boundary conditions are the driving force in our calculations and may do work on the calculation medium [e.g., *Han and Gurnis*, 1999]. If this work induces significant stresses at the surface it may influence the dynamic topography of our calculations. We performed calculations with various lithospheric viscosities (including the keel) between 10 and 500 times that of the lower mantle. As long as the lithosphere is sufficiently more viscous than the upper mantle, there was very little difference in the resulting surface stresses, hence dynamic topography and geoid, indicating that stresses at the surface are caused by the pressure perturbations in the upper mantle associated with keel structure. Also, our use of periodic inflow/outflow boundary conditions likely minimizes this effect. While our calculations use surface motions over a passive mantle, mantle flow beneath a fixed keel could produce similar pressure gradients. The important quantity is the net shear between the surface and the underlying mantle which could be influenced by buoyancy-driven flow, such as subduction. Accordingly we examined mantle flow beneath Australia from a global mantle flow model driven by both plate motion and mantle buoyancy [see *Zhang et al.*, 2010] to investigate whether the velocity boundary conditions assumed at the top and bottom are valid. While this is discussed further in section 5.4, the results are broadly consistent with what we assume in this regard.

[17] We use the upper mantle shear velocity tomography model CUB2.0 [*Shapiro and Ritzwoller*, 2002] to create lithospheric keel thickness distributions for our calculations (Figure 2a). Since the Australian continent is surrounded by relatively

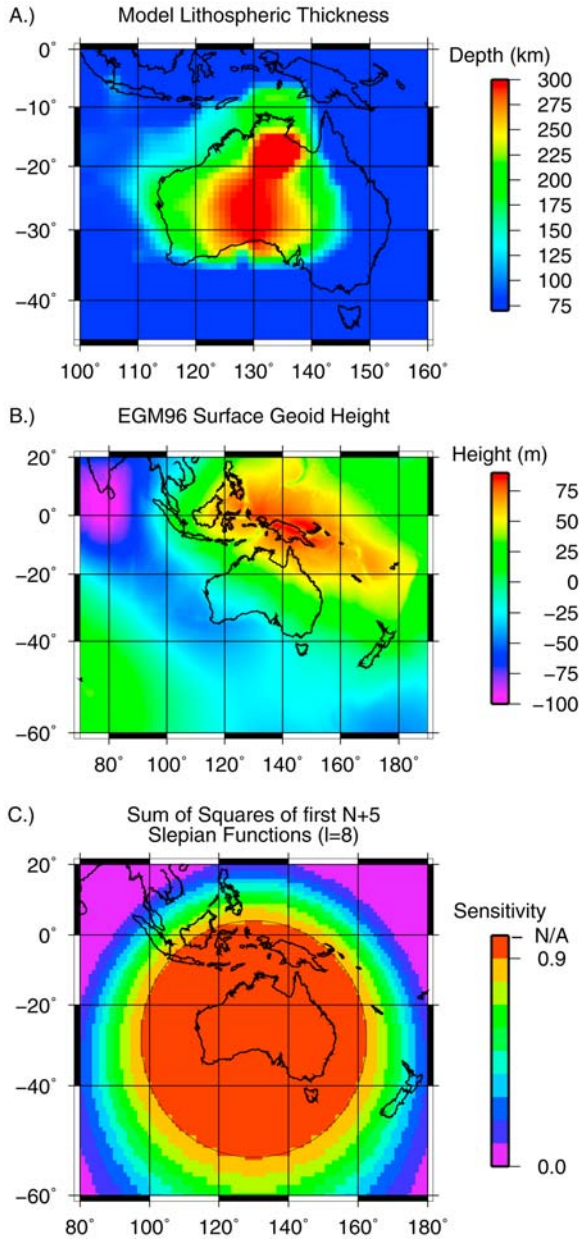

Figure 2. (a) Plot of keel depth from the tomography model CUB2.0 [*Shapiro and Ritzwoller*, 2002]. We map the +2% shear wave speed perturbation from initial model ak135 using V_{SV} and set a maximum lithosphere depth of 300 km. (b) Colored EGM96 geoid height without the degree $l = 2$ zonal spherical harmonic coefficient. (c) Plot of the sum of squares $\sum_{\alpha=1}^{N+5} g_\alpha^2$ of the first $N + 5$ eigenfunctions localized within a 30° circular region centered in western Australia for the bandwidth $L = 0$–8. The colored field shows the sensitivity of our filter to the region of interest. Overlain is the 90% contour of this sensitivity.

young oceanic lithosphere [*Müller et al.*, 2008], lithospheric thickness is set to a minimum of 70 km. At each increasing depth we use a +2% cutoff shear wave velocity perturbation contour with respect to the ak135 reference model [*Kennett et al.*, 1995] to estimate the extent of the continental keel. As mentioned earlier, estimates for the thickness of continental cratonic lithosphere from seismic tomography depend on the type of data used. The CUB2.0 model was created via a Monte Carlo inversion of global surface wave dispersion data using both Rayleigh and Love waves. *Shapiro and Ritzwoller* [2002] specifically allow for radial anisotropy in their inversion, down to a depth of 250 km. Where possible, we use the best fitting V_{SV} estimate, which is consistently smaller than the V_{SH} estimate. Below this depth their data is unable to constrain radial anisotropy and the estimated isotropic shear wave speed, V_S, is used. We limit the thickness of the lithosphere to 300 km since greater thicknesses are not supported by the majority of tomographic upper mantle models.

[18] Our models use layered viscosity structures according to the schematic shown in Figures 1c and 1d. Mantle viscosities are constant with depth within each layer and are rendered dimensionless by a reference value of 2×10^{21} Pa s. Lithospheric viscosity and keel viscosity, are set to a constant significantly higher than the mantle (e.g., 10^{24} Pa s). We begin with a two-layered mantle with viscosity contrast at 670 km and vary the ratio of viscosities of the lower and upper mantle. Calculations are then performed with a three-layered mantle with divisions at 670 km and 400 km depth. Finally, our experiments also vary the thickness of the asthenospheric channel from 50 to 150 km to examine the trade-off between channel viscosity and thickness.

4. Analysis of Gravity

[19] We seek to compare the dynamic geoid anomalies in our calculations to Earth's observed geoid in an effort to constrain the viscosity structure of the upper mantle. This task is neither simple nor straightforward. The Earth's gravitational potential at a given surface point receives contributions from the mass distribution at all depths beneath and around it. In the Australasian region (Figure 2b) we would therefore expect the geoid [*Lemoine et al.*, 1998] to reflect the mass redistribution processes that occur in the surrounding subduction zones [*McAdoo*, 1981], and processes in the lower mantle [*Hager and Richards*, 1989], in addition to the dynamic signal that we must thus attempt to iso-

late. Fortunately, we expect our dynamic signals to be localized both spatially and spectrally. By examining equivalently localized contributions to Earth's gravitational potential field we can distinguish possible dynamic signals from these other regional contributions.

[20] The usual spherical harmonic representation of potential fields links spatial and spectral information through global spherical basis functions which have perfect frequency selectivity but none in space [e.g., *Freeden and Michel*, 1999]. In order to isolate a spatially localized contribution to the signal, spectral and spatial concentration must be balanced somehow.

[21] For instance, *Simons and Hager* [1997] developed a procedure that constrains regional contributions to global spherical harmonic spectra to examine the rebound of the Canadian shield after removal of its ice sheet. They constructed isotropic bandlimited windowing functions on domains with circular symmetry from zonal spherical harmonics, according to a sensible but nonoptimal [see, e.g., *Wieczorek and Simons*, 2005] concentration criterion. After their pioneering work, *Simons et al.* [2006] showed how to derive a family of optimally concentrated basis functions on domains with arbitrarily irregular boundaries. As their construction uses all of the available spherical harmonics Y_{lm}, of integer degree $l = 0, \ldots, L$, and order $m = -l, \ldots, l$, the "Slepian" basis, g_α, $\alpha = 1, \ldots, (L+1)^2$, as it has come to be known, is a perfect alternative to the spherical harmonics. Indeed, any scalar geophysical function, $s(\hat{\mathbf{r}})$, that is bandlimited to degree L and lives (without loss of generality) on the surface of the unit sphere can be represented completely equivalently in either basis,

$$s(\hat{\mathbf{r}}) = \sum_{l=0}^{L} \sum_{m=-l}^{l} s_{lm}\, Y_{lm}(\hat{\mathbf{r}}) = \sum_{\alpha=1}^{(L+1)^2} s_\alpha\, g_\alpha(\hat{\mathbf{r}}). \tag{9}$$

[22] The Slepian functions, g_α, which are bandlimited to some degree L, are always constructed with reference to a particular spatial region of interest, R, of area A, on the surface of the unit sphere, Ω. The criterion for concentration to the region of interest is quadratic: the Slepian functions are those that maximize their energy locally for the available bandwidth, following

$$\lambda = \frac{\int_R g_\alpha^2(\hat{\mathbf{r}})\, d\Omega}{\int_\Omega g_\alpha^2(\hat{\mathbf{r}})\, d\Omega} = \text{maximum}, \tag{10}$$

and where $1 > \lambda > 0$. Practically, they are given by the spherical harmonic expansion

$$g_\alpha(\hat{\mathbf{r}}) = \sum_{l=0}^{L} \sum_{m=-l}^{l} g_{\alpha\, lm} Y_{lm}(\hat{\mathbf{r}}), \tag{11}$$

where the coefficients, $g_{\alpha\, lm}$, are obtained by solving the eigenvalue equation

$$\sum_{l'=0}^{L} \sum_{m'=-l'}^{l'} D_{lm,l'm'} g_{l'm'} = \lambda\, g_{lm}. \tag{12}$$

The four-dimensional object whose elements $D_{lm,l'm'}$ are products of spherical harmonics, integrated over the region R, is called the localization "kernel" [*Simons et al.*, 2006].

[23] The eigenvalues of this problem, λ_1, λ_2, …, $\lambda_{(L+1)^2}$, sum to a space-bandwidth product termed the "spherical Shannon number," N. Typically, N is a good estimate of the number of significant eigenvalues, and thus of the number of well-concentrated functions for the problem at hand. As a result, an expansion of the signal in terms of its first N Slepian functions provides a high-quality regional approximation to the signal in the region [*Simons and Dahlen*, 2006], at the bandwidth level L. Since

$$N = (L+1)^2 \frac{A}{4\pi}, \tag{13}$$

where $A/(4\pi)$ is the fractional area of localization, the effective dimension of the Slepian basis is much reduced compared to the $(L+1)^2$ terms in the spherical harmonic expansion. The Slepian functions are efficient for the study of geographically localized geophysical signals, which are sparse in this basis [*Simons et al.*, 2009],

$$s(\hat{\mathbf{r}}) \approx \sum_{\alpha=1}^{N} s_\alpha\, g_\alpha(\hat{\mathbf{r}}) \quad \text{for} \quad \hat{\mathbf{r}} \in R. \tag{14}$$

[24] The geoid in the region of Australia (Figure 2b) is dominated by two striking features: a broad and large-amplitude positive anomaly to the north near Indonesia and the Western Pacific, and an equally broad and large-amplitude negative anomaly south of India trending to the southeast. Both anomalies are rather long-wavelength features, and can be attributed to the history of subduction and lower mantle structure in the area [e.g., *Hager and Richards*, 1989; *Ricard et al.*, 1993]. A simple estimate for the size of a dynamic keel-related (i.e., model-generated) signal would be roughly the size of the keel itself. Therefore, we shall determine

spatiospectrally localized functions to remove the longer-wavelength contributions to the regional geoid in and around Australia both in the observations and in our model domain, thereby hopefully preserving the signal. By removing the long-wavelength geoid contributions and ascribing what remains to the keel movement we run the risk of incurring bias from an unexpected contribution to the geoid in our analysis. However, the unique spatial pattern in our modeled geoid and its agreement with the filtered observed geoid supports our modeling approach.

[25] We elect to use our functions to remove bandwidths below $L = 8$. This roughly corresponds to the wavelength of our keel outline and our experience has shown that it acceptably balances removing broad, regional geoid features with the preservation of sufficient model signal for analysis. We separate the observations into a low-degree and a high-degree part in both the spherical harmonic and the Slepian basis of bandwidth L, as

$$s(\hat{\mathbf{r}}) = \sum_{l=0}^{L_{\max}} \sum_{m=-l}^{l} s_{lm}\, Y_{lm}(\hat{\mathbf{r}}), \tag{15}$$

$$= \sum_{l=0}^{L} \sum_{m=-l}^{l} s_{lm}\, Y_{lm}(\hat{\mathbf{r}}) + \sum_{l=L+1}^{L_{\max}} \sum_{m=-l}^{l} s_{lm}\, Y_{lm}(\hat{\mathbf{r}}), \tag{16}$$

$$= \sum_{\alpha=1}^{(L+1)^2} s_\alpha\, g_\alpha(\hat{\mathbf{r}}) + \sum_{l=L+1}^{L_{\max}} \sum_{m=-l}^{l} s_{lm}\, Y_{lm}(\hat{\mathbf{r}}). \tag{17}$$

$$= \sum_{\alpha=1}^{N} s_\alpha\, g_\alpha(\hat{\mathbf{r}}) + \sum_{\alpha=N+1}^{(L+1)^2} s_\alpha\, g_\alpha(\hat{\mathbf{r}}) + \sum_{l=L+1}^{L_{\max}} \sum_{m=-l}^{l} s_{lm}\, Y_{lm}(\hat{\mathbf{r}}). \tag{18}$$

Compared to the original expansion (15), equation (18) represents the signal with the low-degree components separated into local (the first term) and nonlocal (the second term) contributions. The first term in equation (18) can thus be omitted in order to remove the local contributions to the low-degree signal.

[26] If we sum the squares of all of the Slepian functions the value N/A is reached everywhere on the unit sphere [*Simons et al.*, 2006]; by performing the partial sum of the first N terms we obtain

$$\sum_{\alpha=1}^{N} g_\alpha^2(\hat{\mathbf{r}}) \approx \frac{N}{A} \quad \text{for} \quad \hat{\mathbf{r}} \in R. \tag{19}$$

By plotting the sum of the first several squared Slepian eigenfunctions we can determine where the truncated expansion is most sensitive and thus most successful at subtracting regional contributions. We will target our attention to the area where the analysis reaches 90% of its maximum sensitivity by this measure. In practice, this means that we shall take the first $N + 5$ basis functions to guarantee the efficient removal of low-degree signal from the region of interest (Figure 2c).

[27] When the geoid is bandlimited to increasingly higher spherical harmonic degrees, shorter-wavelength signals begin to dominate the field. Around Australia, the sharp density contrast between the continental lithosphere and oceanic lithosphere that is over 100 Ma old results in prominent geoid anomalies along the coastline in the shorter-wavelength geoid field. We apply a simple, approximate, correction for these anomalies, derived by *Haxby and Turcotte* [1978]. This correction assumes that topography and bathymetry follow Airy isostatic compensation, and therefore it expresses the change in the moment of the density distribution that is expected when the thickness of crust varies. We apply this correction to the geoid from the EGM96 model [*Lemoine et al.*, 1998] prior to the Slepian filtering technique.

[28] We illustrate the application of our method in Figure 3 using data from EGM96. The Slepian functions we use will be designed to fit the localized power at the low degrees of the geoid. They are bandlimited to $L = 8$ and are concentrated within a region of interest of colatitudinal radius $\Theta = 30°$ centered on colatitude $\theta_0 = 115°$ and longitude $\phi = 130°$ (i.e., the center of the Australian keel). The corresponding rounded Shannon number $N = 5$. Figures 3a–3c display various versions of the EGM96 geoid height that are simply truncated, namely, after removal of the degrees l through 2, through 8, and between 9 and 360, respectively, i.e.,

$$s_1 = \sum_{l=3}^{360} \sum_{m=-l}^{l} s_{lm}\, Y_{lm}, \tag{20}$$

$$s_2 = \sum_{l=9}^{360} \sum_{m=-l}^{l} s_{lm}\, Y_{lm}, \text{ and} \tag{21}$$

$$s_3 = \sum_{l=3}^{8} \sum_{m=-l}^{l} s_{lm}\, Y_{lm}. \tag{22}$$

For reference we note that s_1, in Figure 3a, is a fair approximation to the Earth's nonhydrostatic geoid.

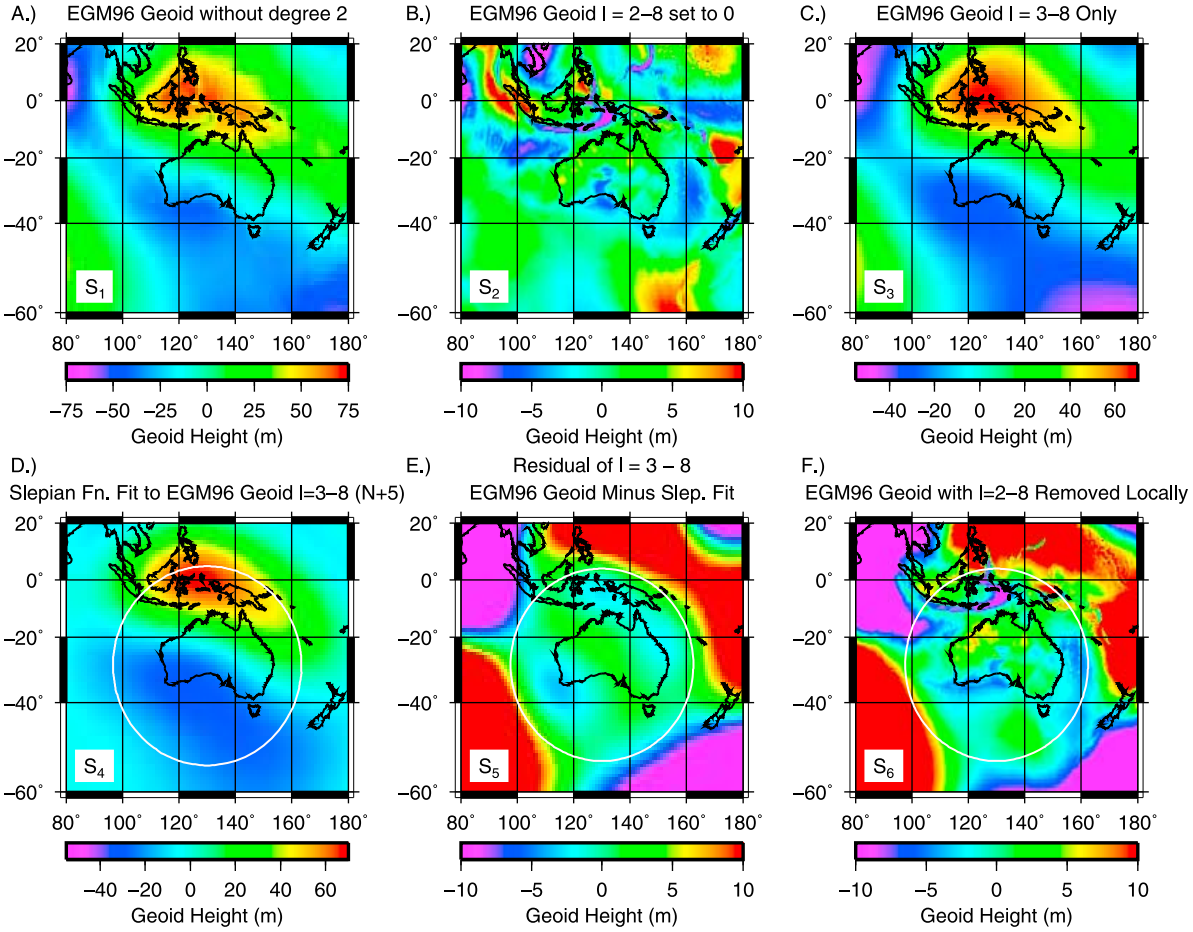

Figure 3. Example of Slepian filtering technique for a low maximum bandwidth of $L = 8$. (a–c) Spectrally truncated versions of the EGM96 geoid height. (d–f) The filtering process. Figure 3a shows the complete EGM96 geoid undulation with degree $l = 2$ removed. Figure 3b shows the geoid with all coefficients from $l = 2$ through $l = 8$ set to zero. Figure 3c shows the geoid between $l = 3$ and 8. In this example, our functions are designed to fit the localized power of these low degrees. Figure 3d shows the fit of the first N+5 Slepian eigenfunctions to the low-degree EGM96 geoid (Figure 3c), concentrated within a 30° circular region (outlined in white) centered over western Australia. Figure 3e shows the residual after subtracting the Slepian fit from the low-degree EGM96 geoid. Overlain in white is the 90% contour of sensitivity from Figure 2c. Figure 3f shows the results of subtracting the low-degree Slepian fit from the full EGM96 geoid (Figure 3a). Figures 3b, 3e, and 3f are shown with the same color scale, as are Figures 3c and 3d.

[29] In the course of our analysis we found that reconstructing the low-degree geoid with a Slepian basis of more than N terms was necessary to obtain good fits to the modeled data. Therefore, Figures 2c and 3d–3f use $N + 5 = 10$ basis functions to remove the local signal. Including these extra functions does not significantly affect the trade-off between spatial and spectral localization. In Figures 3d–3f we show the filtering process by first showing, in Figure 3d, the fit of the first $N + 5$ Slepian eigenfunctions to the low-degree EGM96 geoid (i.e., s_3 shown in Figure 3c), with the circular region of concentration, the 90% contour of sensitivity that is also shown in Figure 2c, outlined in white. Figure 3e displays what remains after subtracting the Slepian fit from the low-degree EGM96 geoid, s_3 shown in Figure 3c. Finally, Figure 3f shows the results of subtracting the low-degree Slepian fit (i.e., Figure 3d) from the full EGM96 geoid shown in Figure 3a. In other words, we are plotting

$$s_4 = \sum_{\alpha=1}^{10} s_\alpha g_\alpha, \tag{23}$$

$$s_5 = \sum_{\alpha=11}^{81} s_\alpha g_\alpha = s_3 - s_4, \text{ and} \tag{24}$$

$$s_6 = \sum_{\alpha=11}^{81} s_\alpha g_\alpha + \sum_{l=9}^{360} \sum_{m=-l}^{l} s_{lm} Y_{lm} = s_1 - s_4. \tag{25}$$

A comparison of s_2 and s_6 in Figures 3b and 3f, which are shown using the same color scale, shows the changes due to the regional subtraction of low-degree signal. These changes include some subtle changes in geoid height such as slightly broader and larger positive anomalies in northwestern Australia, and broader negative anomalies along the southwestern coast of Australia. This comparison shows the difference between what would be the "traditional" all-spectral and the optimized "Slepian" spatiospectral approach to removing the regional low-degree contributions to the geoid.

[30] In conclusion, spatiospectral filtering allows us to examine the geoid in and around Australia without being biased by power in the $0 \rightarrow L$ degree range that mostly arises from regions outside of Australia. The resulting geoid anomalies from this analysis in the Australian region show a distinct feature with negative and positive anomalies of amplitude of ~10 m in the southern and northern parts of Australia, respectively (Figure 3f). Such regional geoid anomalies are used in this study to constrain mantle viscosity structure.

5. Three-Dimensional Numerical Results

[31] We performed calculations using the keel shown in Figure 2a and varied the viscosity of the asthenosphere. From the vertical normal stress field we calculate the dynamic topography at the surface (Figure 4a) and at the core-mantle boundary, which is then used to calculate surface geoid anomalies (Figure 4b). As upper mantle viscosity is varied, the spatial patterns of topography and the geoid remain roughly the same while the magnitude fluctuates. At the leading edge of the keel, vertical normal stresses cause positive dynamic topography at the surface while near the trailing edge of the keel the reverse is true, with negative dynamic topography at the surface. The resulting geoid anomaly is also positive at the leading edge of the keel and negative at the trailing edge. Some asymmetry also results due to the shape of the lithospheric keel.

[32] While the example model outputs shown in Figures 4a and 4b have yet to be filtered, a similar pattern is seen to occur in the observed geoid after locally removing long wavelengths (Figure 3f). In both modeled and observed fields, broad positive geoid anomalies occur along the coast of northwestern Australia, and broad negative anomalies along the southwestern coast. We explore this behavior further later, but this initial observation provides context for some of our model results.

5.1. Two-Layered Mantle

[33] The primary descriptor of our model results is the magnitude of the dynamic geoid anomaly. In a two-layer mantle with a division at 670 km depth (Figure 4c), the anomaly magnitudes vary with the thickness and viscosity of the channel below the keel. When the viscosity of the entire mantle is uniform (Figure 4c, dashed line), the channel below the keel is effectively very thick, and the magnitude of the dynamic geoid anomaly (Figure 4c) is relatively small (contours indicate the maximum geoid anomalies reached). As upper mantle viscosity decreases, this channel effectively gets thinner as deformation concentrates in the upper mantle, and the geoid anomaly increases. This increase continues until the viscosity contrast reaches approximately 1:33 (third row of squares below dashed line). Eventually the low viscosity of the upper mantle is the dominant property, reducing stress and geoid magnitudes. This is similar to what we observed from the simple analytical models plotted in Figure 1b.

5.2. Three-Layered Mantle

[34] In a three-layered mantle, the general results from two-layer models remain valid. For a constant lower mantle viscosity (3×10^{22} Pa s in Figure 4d), when upper mantle (<400 km depth) viscosity is reduced relative to the transition zone (between 400 and 670 km depth), geoid anomalies initially increase as more flow is concentrated in the upper mantle. As upper mantle viscosity is decreased further, the dynamic geoid anomalies are eventually reduced as the low viscosity reduces stress magnitudes. The effect of the weak channel is also apparent here more explicitly. In Figure 4d, the diagonal dashed line is for an upper mantle and transition zone that have equal viscosities, which corresponds again to a two-layer system with division at 670 km depth. Alternatively, the vertical dashed line denotes cases where the transition zone and lower mantle are isoviscous. This represents a two-layer system with division at 400 km depth. Cases near the division at 400 km generally result in larger anomaly magnitudes, except for two regions: (1) when mantle viscosity is nearly uniform (top right of Figure 4d) the channel is thick enough to dominate subtle changes in viscosity

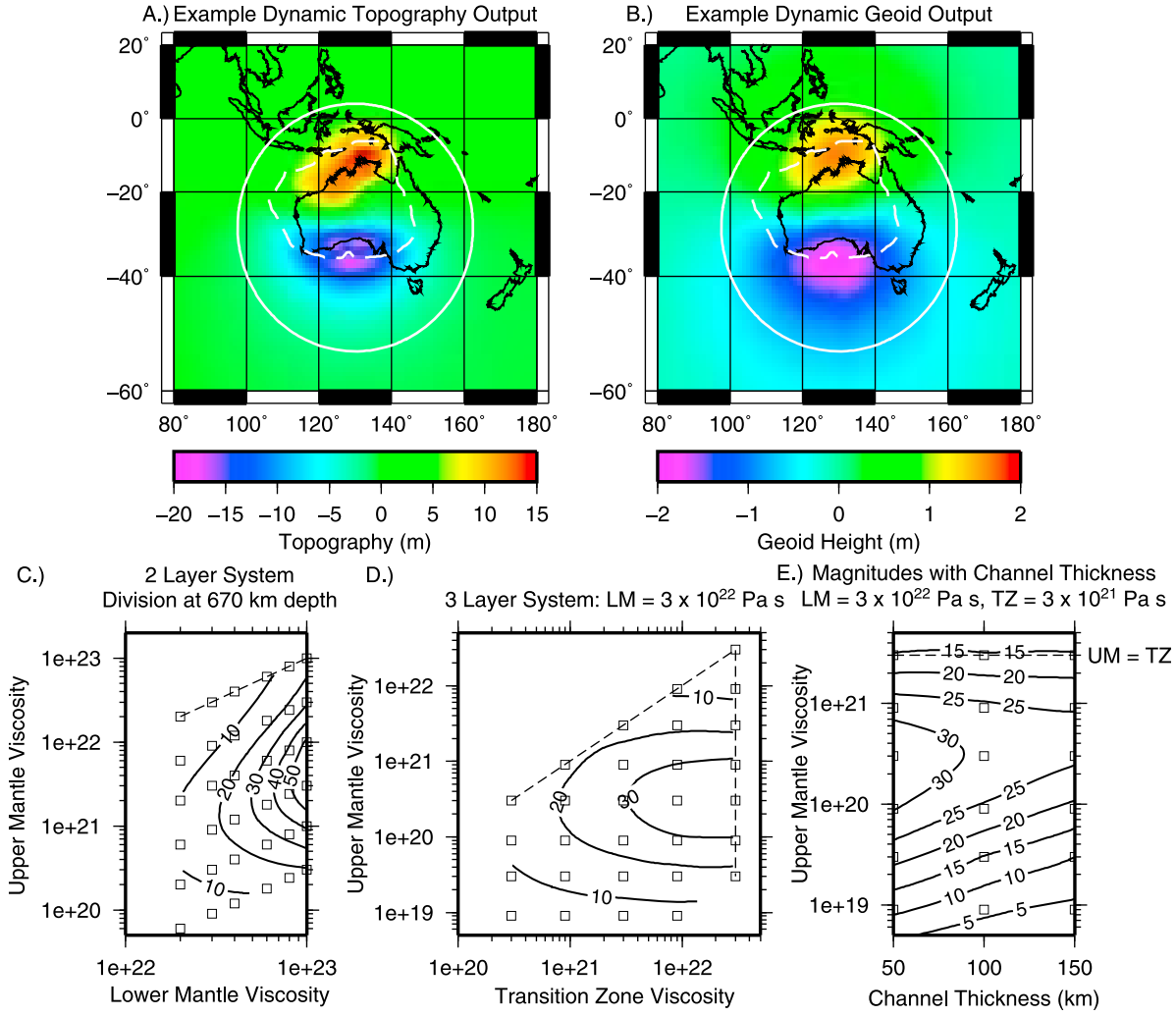

Figure 4. Examples of model output. (a) Example dynamic topography at the surface for a calculation with η_{LM} = 3 × 10^{22} Pa s, η_{TZ} = 3 × 10^{21} Pa s, and η_{UM} = 3 × 10^{20} Pa s. The colored topography anomalies are scaled to a surface velocity of 1 cm/yr. The surface velocity vector is aligned with the plate motion vector at azimuth 1.81° from north. In solid white we show the 90% contour of filter sensitivity from Figure 2c. In dashed white we show the outline of the Australian keel (where thickness >100 km) determined from the CUB2.0 model. (b) Example dynamic geoid anomalies at the surface from the same calculation, also scaled to 1 cm/yr of surface motion. (c–e) Contoured magnitudes of unfiltered model geoid anomalies in m, scaled to the Australian surface motion of 8.267 cm/yr. Magnitude simply represents the difference between peak minimum and maximum anomaly (i.e., no pattern information, about 3.6 m in Figure 4b). Hollow squares show model individual runs. Figure 4c shows magnitudes in a two-layered mantle with division at 670 km depth. Figure 4d shows magnitudes in a three-layered mantle with divisions at 670 km and 400 km depth. Here the viscosity of the lower mantle is fixed at 3 × 10^{22} Pa s. Diagonal dashed line is where the upper mantle and transition zone have equal viscosity, equivalent to a two-layered mantle divided at 670 km depth. Vertical dashed line is where the transition zone and lower mantle have equal viscosity, equivalent to a two-layered mantle divided at 400 km depth. (e) Contoured magnitudes of unfiltered model geoid anomalies in m for different channel thicknesses. Lower mantle and transition zone viscosities are fixed at 3 × 10^{22} Pa s and 3 × 10^{21} Pa s, respectively. Horizontal dashed line shows where the upper mantle and transition zone are isoviscous.

structure and (2) when the viscosity of the weakest layer is low (bottom of Figure 4d), stress magnitudes are low enough that changing channel thickness results in an insignificant change to anomaly magnitude.

5.3. Channel Flow

[35] Arguably, the controlling parameter of this process is not the absolute depth of the continental keel, but the thickness of the asthenospheric chan-

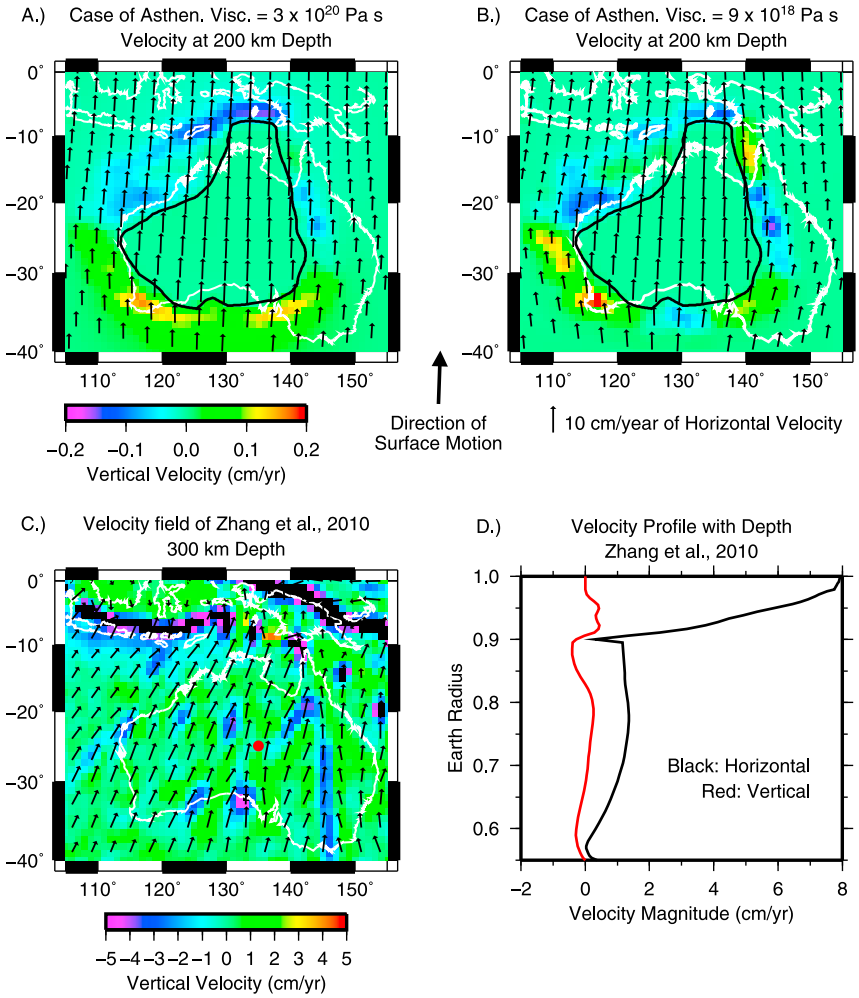

Figure 5. Mantle velocity at 200 km depth for two model cases. Vectors show horizontal velocity. Colors show vertical velocity, with positive values out of the page. The 10 cm/yr scale vector for horizontal motion is valid for Figures 5a–5c. Coastlines are outlined in white. In both cases, $\eta_{LM} = 3 \times 10^{22}$ Pa s and $\eta_{TZ} = 3 \times 10^{21}$ Pa s. The depths shown are at 200 km, and the black shape outlines the Australian continental lithosphere at this depth. (a) A case with asthenospheric viscosity $\eta = 3 \times 10^{21}$ Pa s. (b) A case with asthenosphere viscosity $\eta = 9 \times 10^{18}$ Pa s. (c) Similar velocity slice at 300 km depth from a global mantle flow model of *Zhang et al.* [2010]. Note the different scale for vertical velocity; magnitudes less than −5 cm/yr are black. (d) Vertical profile of velocity with depth for point in Figure 5c indicated by red dot (135°E, 25°S).

nel. Different keel thicknesses can combine with regional variations in the depths of upper mantle discontinuities to change the thickness of the asthenospheric channel below it [e.g., *Gilbert et al.*, 2001].

[36] Accordingly, we performed calculations varying the thickness and viscosity of this channel (Figure 4e). Once again, we contour the maximum resulting geoid anomalies. Channel thickness is varied by adjusting the depth to the asthenosphere–transition zone viscosity contrast to examine cases with 50 km, 100 km, and 150 km between this boundary and the keel bottom, while keeping the keel thickness at 300 km. Generally, an increase in channel thickness results in a smaller geoid anomaly, as expected. This change is smaller than one might expect, however, from a single-layer model (equation (4)), or even a two-layered mantle (equation (6) and Figure 1), where pressure gradients are nonlinearly (e.g., cubically in uniform viscosity mantle models) related to channel thickness. Instead, in 3-D it seems likely that this nonlinearity is offset by flow that passes relatively unconstrained around the sides of the keel region.

5.4. Flow Field

[37] As a continental keel moves through a less viscous upper mantle we might expect the mantle

to deform horizontally around the sides of the keel [*Fouch et al.*, 2000] or vertically, beneath the keel. The largest expected control on this deformation is the viscosity of the asthenosphere, and hence, in Figure 5, we show horizontal (vectors) and vertical velocity (colors) at a depth in the asthenosphere for two of our cases, one with moderate and one with low asthenosphere viscosity. Surprisingly, both cases are fairly similar.

[38] The case with moderate asthenospheric viscosity ($\eta = 3 \times 10^{20}$ Pa s) displays very little variation of velocity with latitude (Figure 5a). This case also shows downgoing velocities at the leading, and rising velocities at the trailing edge of the keel, indicating that material predominantly flows beneath the keel rather than horizontally around it.

[39] While the case with lower asthenospheric viscosity ($\eta = 9 \times 10^{18}$ Pa s) does show variation in the plane (Figure 5b), with velocity vectors deflected around the keel, these discrepancies do not exceed ten degrees from the azimuth of surface motion. This second case also has vertical velocities that are similar to those in the first case, but with somewhat more variability. It is not until asthenospheric viscosity is decreased even further that flow directions start to significantly deviate from the direction of plate motion.

[40] Since flow in the mantle could affect the net flow across the keel, or perhaps vertically beneath it, we examine the velocity field beneath Australia from a global mantle convection model [*Zhang et al.*, 2010, case FS1]. The model, shown for the present day in planform in Figure 5c and in profile in Figure 5d, is the result of a time-dependent calculation and includes both prescribed surface plate motion history and mantle buoyancy forces. The modeled horizontal motion in the mantle is broadly consistent with our own model assumptions: motion in the mantle, particularly in the high-viscosity lower mantle, is low relative to the motion at the surface and is a good representation of the net shear across the mantle. North of Australia, the vertical motion in the upper mantle is dominated by the subduction zones that have velocity magnitudes near −8 cm/yr. Under Australia there are several small-scale downwellings below the lithosphere, which are likely due to sublithospheric small-scale convection aided by large plate motion [e.g., *van Hunen et al.*, 2005]. Both types of vertical motion could influence the keel-induced pressure gradient, and should therefore be taken into account when making interpretations.

6. Geoid Comparison With Observations

[41] To constrain the upper mantle viscosity structure we compare the dynamic geoid from our model calculations to the Earth's observed geoid. Since our data are localized spatially as well as spectrally, and because Earth's gravitational potential receives many different contributions across the spatial and spectral domains we apply the Slepian filtering technique discussed in section 4 to both model and observations before comparing them.

6.1. Two-Layered Mantle

[42] We begin by comparing geoids from our two-layer models with the observed geoid. We calculate the misfit by finding the 2-D absolute value of the error per measurement as

$$\text{Misfit} = \frac{1}{n}\sum_{i=1}^{n}|\text{obs}_i - \text{model}_i| \tag{26}$$

where obs_i is an observed geoid measurement at a specific location, model_i is a model geoid measurement at the same location, and n is the total number of values compared (which is identical in every case studied). Misfit is calculated within a subregion that includes our largest-amplitude model geoid anomalies (Figure 6a, dashed rectangle), excluding areas where model anomalies are low. This area covers both continental and oceanic parts of the Australian region. If we were to examine a null model, equation (26) will produce a misfit that represents the inherent power of the observed field, approximately 3 m. For our cases, models with misfit values below this fit the observed field better than a null model.

[43] When inspecting misfit for a two-layered mantle (Figure 7a), three scenarios emerge. First, a model that produces minimal dynamic geoid anomalies, such as a uniform mantle of viscosity 2×10^{22} Pa s, will produce a misfit around 3 m. Second, a model that reproduces the observed field results in a minimum misfit. This can be seen in model case A in Figures 6b and 6c, whose residuals remain fairly uniform from north to south and have small amplitudes. Finally, a model that produces very large geoid anomalies will overshoot the

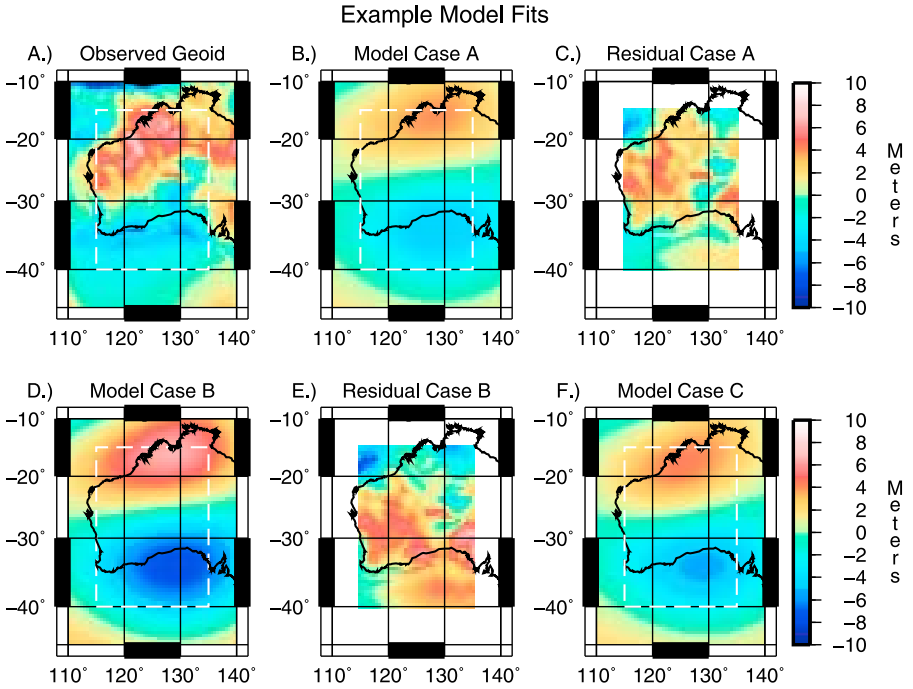

Figure 6. Example model fits. Example cases are denoted by red squares in Figure 7. Model cases A and B are for a two-layered mantle, while case C is from a three-layered mantle. Model cases are subtracted from the observed geoid field within the dashed white box, yielding the plots of residuals. The dashed white box also marks the area used for calculating misfit. All geoid fields are plotted using the same ±10 m scale. (a) Filtered observed geoid field. (b) Filtered model geoid from case A for a two-layered mantle. (c) Residual for case A. (d) Filtered model geoid from case B for a two-layered mantle. (e) Residual for case B. (f) Filtered model geoid from case C for a three-layered mantle. This example is similar to case A, and a residual is not shown.

apparent signal in the observed field (model case B in Figures 6d and 6e). While the average magnitude of this misfit is of the same order as that from a model with null signal, upon inspection it is clear that the positive-negative north-south signature of the residual has reversed.

[44] The misfit for a two-layered mantle reaches an absolute minimum when the lower mantle viscosity $\eta_{LM} = 5.3 \times 10^{22}$ Pa s and the upper mantle viscosity is about 20 times smaller, $\eta_{UM} = 2.75 \times 10^{21}$ Pa s. It is clear from Figure 7a, though, that there is a broad region with misfits near the minimum where models can be considered acceptable. The trade-off between effective channel thickness and upper mantle viscosity implies that models with viscosity increases from the upper to the lower mantle with ratios between 3 and 300 could be considered supported by the data. In a two-layered mantle, the viscosity jump between the upper and lower mantle cannot therefore be sufficiently constrained.

6.2. Three-Layered Mantle

[45] In a three-layered mantle, we fix lower mantle viscosity and plot how misfit varies for different viscosities of the upper mantle and transition zone (Figures 7b and 7c). As described earlier, when a weak upper mantle layer is introduced, dynamic geoid anomalies can increase. Here, this means that we should expect more variation in the pattern of misfit depending on the viscosity structure.

[46] When lower mantle viscosity is 2×10^{22} Pa s (Figure 7b), the dynamic geoid anomalies generally have low magnitudes. The minimum misfit suggests a structure that maximizes the dynamic geoid signal. Thus a structure with an upper mantle viscosity of 1–2 $\times 10^{20}$ Pa s (about 100 times weaker than the lower mantle) and a transition zone viscosity of 3–10 $\times 10^{21}$ Pa s is preferred.

[47] At lower mantle viscosities higher than 2×10^{22} Pa s, overall anomaly magnitudes increase, e.g., to the values already shown in Figure 4d, and the misfit pattern becomes more intricate (Figure 7c).

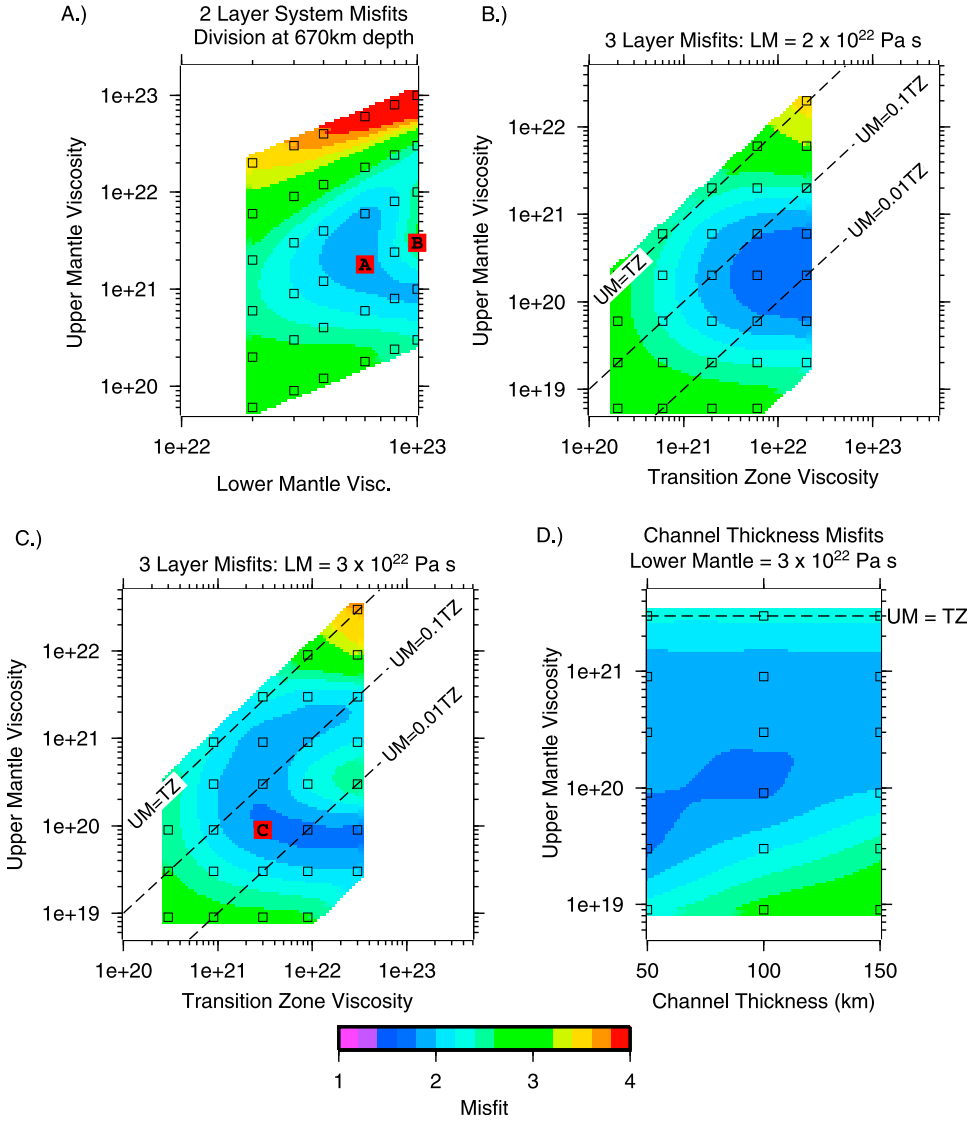

Figure 7. Color-shaded images of misfit between filtered model cases and observed geoid. Hollow squares identify model runs. The background observed geoid field has a mean power of about 3.1 m. Therefore, the misfit between the observed field and a model with no (zero) geoid anomaly would be about 3.1 m. This occurs when upper mantle viscosity is very low ($<10^{19}$ Pa s). Other instances of misfit about 3.1 m occur when model signal is roughly twice the power (i.e., the model signal overshoots the observed signal, resulting in a residual with power equivalent to the original observed field). (a) Model misfits for a two-layered mantle with division at 670 km depth. Red squares A and B denote cases shown in Figure 6. (b) Model misfits for a three-layer mantle with lower mantle viscosity held fixed at 2×10^{22} Pa s. (c) Model misfits for a three-layer mantle with lower mantle viscosity fixed at 3×10^{22} Pa s. Red square denotes case C shown in Figure 6. (d) Model misfits for a three-layered mantle for varying channel thicknesses. Channel thickness is determined by varying the depth to the upper mantle–transition zone viscosity discontinuity. Lower mantle and transition zone viscosities are fixed at 3×10^{22} Pa s and 3×10^{21} Pa s, respectively. Dashed line indicates where the upper mantle and transition zone are isoviscous.

Regions of lowest misfit generally occur when $\eta_{UM} < 10^{20}$ Pa s. For the cases shown where $\eta_{LM} = 3 \times 10^{22}$ Pa s, the absolute minimum misfit occurs when $\eta_{TZ} = 2.7 \times 10^{22}$ Pa s and $\eta_{UM} = 7.9 \times 10^{19}$ Pa s, but the region of misfits near this minimum is in fact quite broad. If we examine only the cases with misfits <1.8 m (the darkest shades of blue in Figure 7c), we can make some interesting further observations about the best fitting viscosity structure. In each of these cases there

is a factor of ~300 between the viscosities of the lower and upper mantle. Meanwhile, the viscosity of the transition zone varies over an order of magnitude, indicating that it is less important once the upper mantle is sufficiently weak. We show such a model case with three layers that has a low misfit (<1.8 m, see Figure 7c) in Figure 6f (model case C). While the pattern of the model signals remains fairly consistent between the two and three-layered cases, the changes in amplitude cause the best fits to shift to lower upper mantle viscosities.

[48] Finally, we examine the effects of the thickness of the asthenospheric channel on the model geoid using a set of calculations in which asthenospheric viscosity and channel thickness are varied while transition zone and lower mantle viscosities are fixed at 3×10^{21} Pa s and 3×10^{22} Pa s, respectively (Figure 7d). The misfit in these models is less sensitive to asthenospheric channel thickness than one might expect from the single-layer analysis (equation (4)). This confirms the finding that lateral flow of mantle material around the sides of lithospheric keels plays a role in the upper mantle.

7. Discussion

7.1. Constraints on Mantle Viscosity Structure

[49] Two classic methods to study mantle viscosity make use of observations associated with postglacial rebound, and long-wavelength geoid anomalies. Generally, in studies of postglacial rebound, the Earth's response to surface loads is modeled and fit to observations such as relative sea level histories [*Peltier*, 1976; *Wu and Peltier*, 1982; *Mitrovica*, 1996; *Simons and Hager*, 1997; *Peltier*, 1998; *Mitrovica et al.*, 2007] or time-varying gravity anomalies from the Gravity Recovery and Climate Experiment (GRACE) [*Paulson et al.*, 2007a; *Tamisiea et al.*, 2007]. In some long-wavelength studies, geoid anomalies from the mantle's internal density variations, which depend on the viscosity structure, are compared to the observed geoid [e.g., *Hager and Richards*, 1989]. While studies of long-wavelength geoid anomalies have suggested a lower mantle that is significantly more viscous than the upper mantle [e.g., *Hager*, 1984; *Ricard et al.*, 1984; *Hager and Richards*, 1989], the results of postglacial rebound studies are not always consistent among themselves, with some suggesting a more uniform mantle viscosity [e.g., *Peltier*, 1998], and others also arguing for a lower mantle that is significantly stronger than the upper mantle [e.g., *Lambeck et al.*, 1990; *Han and Wahr*, 1995; *Simons and Hager*, 1997; *Mitrovica and Forte*, 2004]. Using relative sea level change and GRACE time-varying gravity data, *Paulson et al.* [2007a, 2007b] recently showed that the inconsistency among the postglacial rebound studies owes to the poor depth resolution of the observations. In particular, *Paulson et al.* [2007a] showed that if the mantle is divided into two layers with division at 670 km depth, viscosity models that have $\sim 5 \times 10^{19}$ Pa s and $\sim 5 \times 10^{22}$ Pa s for the upper and lower mantle, respectively, produce fits to both data types that are similar to those of a viscosity model with 5.3×10^{20} Pa s for the upper and 2.3×10^{21} Pa s for the lower mantle.

[50] The main objective of this study has been to seek additional constraints on upper mantle viscosity by examining the gravity anomalies caused by the pressure difference associated with moving Australian continental lithosphere, a thick keel plowing through the mantle. Our study therefore represents a new method to constrain the viscosity structure of the mantle. We found that modeled geoid anomalies caused by a moving continental lithosphere with a keel show remarkable similarities to the observations, with negative and positive geoid anomalies in southern and northern Australia, respectively. Assuming that such geoid anomalies are indeed caused by the pressure difference induced by the keel's motion, we have shown that geoid anomalies, when properly filtered to account for localized, long-wavelength effects, can provide useful constraints on mantle viscosity.

[51] If the mantle is divided at 670 km depth into two layers, the geoid in Australia is best explained by a mantle viscosity structure with 2.75×10^{21} Pa s and 5.3×10^{22} Pa s for the upper mantle and lower mantle, respectively, a factor of 20 increase. However, this viscosity structure does not appear to be consistent with the relative sea level and GRACE data as shown by *Paulson et al.* [2007a]. This difficulty can be resolved by introducing an additional layer or weak asthenosphere from the base of the lithosphere to 400 km depth. We found that such a weak asthenosphere tends to amplify the effects of a continental keel. With our three-layer models, and fixing lower mantle viscosity to values between 2 and 3×10^{22} Pa s, we found that upper mantle viscosity (i.e., above 400 km depth) needs to be $\sim 10^{20}$ Pa s, or ~300 times weaker than the lower mantle, in order to reproduce the geoid anomalies in Australia. Interestingly, this viscosity structure is generally permissible by the relative sea level and GRACE data, as shown by *Paulson et al.* [2007a]. However, our result depends on

the magnitude of lower mantle viscosity. If the lower mantle is too weak (10^{22} Pa s or less), the geoid produced by the keel is too small to explain the observations. Therefore, our study suggests that future geodynamics studies (e.g., on mantle structure, heat transfer, and mantle mixing) and mantle rheology should consider the possibility of relatively high lower mantle viscosity of 2–3 × 10^{22} Pa s.

[52] Recently, *Conrad and Behn* [2010] used seismic anisotropy and lithospheric net rotation to constrain model viscosities for the asthenosphere (down to 300 km depth in their models) and the transition zone (between 300 km and 670 km depths) to be 0.5–1 × 10^{20} Pa s and 0.5–1 × 10^{21} Pa s, respectively, while the lower mantle viscosity is fixed at 5 × 10^{22} Pa s. Considering the difference between our models in dividing the viscosity layers, the viscosities for the upper mantle above 670 km depth from our study are quite similar to those of *Conrad and Behn* [2010]. However, these authors did not explore the dependence of their models on lower mantle viscosity.

7.2. Relevance to Other Continental Keels

[53] The first-order controls on upper mantle pressure gradients in our calculations are the viscosity structure of the mantle and the magnitude of surface velocity. In addition to these primary controls, a set of secondary factors can influence the dynamic topography at the surface to a lesser extent. Our calculations are for a fixed keel size. If the length of the keel is increased (in the direction of surface motion) then the distance between positive and negative dynamic topography will increase, and more power of the geoid anomaly will be at longer wavelengths. If the keel's width is increased (perpendicular to surface motion) then dynamic anomalies widen as well. In this instance magnitudes of dynamic topography will also be larger since a wider keel displaces more mantle as it moves.

[54] One of the unique features of the Australian keel is its asymmetry in the direction of surface motion (Figure 2a). From the thickest part of the lithosphere (at about 130° longitude) to the east, the lithosphere quickly thins, coincidentally with the decrease in crustal age [*Simons and van der Hilst*, 2002]. To the west this transition is more gradual and tends to follow the boundary between continental and oceanic crust (along the western coast). The effect of this asymmetry is most easily seen in the positive dynamic topography at the leading edge of the keel (Figure 4a). Such a shape in other keels could result in unique dynamic geoid anomalies. A unique geoidal pattern would help distinguish pressure-induced anomalies from other processes that could be acting on keel edges such as small-scale or edge-driven convection [e.g., *King and Ritsema*, 2000; *Conrad et al.*, 2010].

[55] Several cratonic regions, such as North America, western Africa, and Siberia [*Artemieva*, 2009], have lithospheric keels as thick as Australia (>250 km). If keel-induced pressure effects could be observed for these regions this could provide additional constraints on mantle viscosity. Each of these regions has relatively slow surface motion that could make it difficult, however, to detect dynamic signals as we did in our analysis. We performed our analysis for Australia because its large surface motion makes it the most likely to show these effects. The keels in western Africa and Siberia have surface speeds below about 2 cm/yr [*Gripp and Gordon*, 2002], so to first order the geoidal anomalies would have much reduced magnitude. While also having low surface speeds of roughly 3 cm/yr, the North American keel could still have detectable anomalies due to its larger keel size.

7.3. Seismic Anisotropy

[56] Viscous deformation in the upper mantle is dominated by the rheology of its most dominant mineral, olivine [*Karato and Wu*, 1993]. This deformation aligns elastically anisotropic olivine crystals [e.g., *Verma*, 1960] in a lattice-preferred orientation [*McKenzie*, 1979; *Ribe*, 1989] in the upper mantle, an effect that is regularly studied seismologically [e.g., *Hess*, 1964; *Forsyth*, 1975; *Long and Silver*, 2009]. Because of this relationship, observations of seismic anisotropy can be used to constrain geodynamic models of mantle flow [e.g., *Conrad et al.*, 2007]. In practice, complexities such as the strain history [e.g., *Ribe*, 1992], "frozen" lithospheric anisotropy [e.g., *Silver*, 1996; *Savage*, 1999; *Silver et al.*, 2001], the presence of water [*Jung and Karato*, 2001], grain boundary effects [e.g., *Zhang and Karato*, 1995], and so on, mean that such constraints are fraught with uncertainty [e.g., *Savage*, 1999; *Kaminski and Ribe*, 2001; *Becker et al.*, 2006]. However, the first-order approach of inferring from the direction of seismic anisotropy the direction of mantle flow has been fruitful, elucidating, for example, patterns of flow around hot spots or underneath oceanic plates [e.g., *Becker et al.*, 2003; *Behn et al.*, 2004; *Walker et al.*, 2005].

[57] Our own results for Australia can be brought to bear on this relationship, by examining our instantaneous flow field velocities in the context of published regional studies of seismic anisotropy, recently summarized by *Fouch and Rondenay* [2006]. Generally, body wave measurements made at seismic stations correlate with the large-scale structure at the surface, suggesting strong lithospheric anisotropy [*Fouch and Rondenay*, 2006]. Surface wave analyses, which provide better constraints on the variation of anisotropy with depth, have been conducted throughout the Australian continent in the past decade [e.g., *Debayle*, 1999; *Debayle and Kennett*, 2000a, 2000b; *Simons et al.*, 2002, 2003; *Debayle et al.*, 2005]. Australia and North America have both been found to have significant (about 2%) azimuthal anisotropy at or below 200 km depth [e.g., *Debayle et al.*, 2005; *Marone and Romanowicz*, 2007]. This deep anisotropy (below 150 km) mostly correlates with present-day plate motion [e.g., *Simons et al.*, 2002; *Simons and van der Hilst*, 2003; *Debayle et al.*, 2005].

[58] As mentioned earlier, we might expect mantle flow to deflect around a continental keel. Based on the pattern of observed shear wave splitting measurements, *Fouch et al.* [2000] have suggested this is the case in North America. At depths of 150 km, *Debayle and Kennett* [2000a] found that anisotropy in western and central Australia aligns with north-south plate motion while eastern Australia displays azimuthal anisotropy that appears to follow the craton boundary. However, deformation akin to that suggested by the anisotropy does not occur in our models unless asthenospheric viscosity is very low ($<9 \times 10^{18}$ Pa s). Our results agree with the large majority of anisotropy measurements at these depths that align in the direction of surface plate motion [e.g., *Debayle and Kennett*, 2000b; *Simons et al.*, 2003; *Debayle et al.*, 2005], and suggests that return flow occurring beneath the keel is important.

8. Conclusions

[59] When continental keels are driven by imposed surface motion, pressure perturbations cause positive dynamic topography at the leading edge, and negative dynamic topography around the trailing edge of the keel. Depending on the viscosity structure of the mantle, this dynamic topography can be on the order of ±100 m and the corresponding geoid anomalies can be on the order of ±10 m.

[60] When filtered to remove localized long-wavelength anomalies using a technique developed using Slepian functions, the Australian geoid clearly displays the expected pattern, with positive and negative anomalies of about 10 m amplitude at the leading and trailing edges of the craton, respectively. Our model results agree with the observations: assuming that the signal is indeed caused by the dynamic motion of the keel, we are able to obtain constraints on the mantle viscosity structure below the continent.

[61] Dynamic topography produced by motion of a continental keel depends strongly on the effective thickness and viscosity of the asthenosphere, where most of the horizontal motion occurs. For a two-layered mantle with a division at 670 km, decreasing upper mantle viscosity can increase dynamic topography if viscosities are large enough. The minimum misfit between the modeled and observed geoid occurs when $\eta_{LM} = 5.3 \times 10^{22}$ Pa s and $\eta_{UM} = 2.75 \times 10^{21}$ Pa s. However, these viscosities appear too large compared with postglacial rebound studies. This suggests that radial mantle viscosity variations are not fully captured by two-layer models.

[62] In a three-layer mantle, misfit patterns become more complex as lower mantle viscosity is increased. For a lower mantle viscosity $\eta_{LM} = 3 \times 10^{22}$ Pa s, the minimum misfit occurs when the upper mantle viscosity $\eta_{UM} = 7\text{–}10 \times 10^{19}$ Pa s, a factor of about 300 smaller than that of the lower mantle, while the transition zone viscosity η_{TZ} may vary between 10^{21} and 10^{22} Pa s. Such a viscosity structure is not inconsistent with postglacial rebound studies. Since our results are sensitive to lower mantle viscosity, they also suggest that a relatively high lower mantle viscosity should be considered in future geodynamic studies.

Notation

A	area of geographical region of interest.
$D_{lm,l'm'}$	spatiospectral localization kernel.
d	thickness of the lower mantle.
d'	dimensionless thickness of the lower mantle.
F	location far from keel for analytical treatment.
g_α	Slepian basis function on the unit sphere.
$g_{\alpha\ lm}$	spherical harmonic coefficients of the Slepian function g_α.
h_0	thickness of the upper mantle.
h	thickness of the low-viscosity channel.

h' dimensionless thickness of the low-viscosity channel.
K location under keel for analytical treatment.
k thickness difference between keel and surrounding lithosphere ($h_0 - h$).
k' dimensionless thickness difference between keel and surrounding lithosphere.
L degree of bandlimit of geophysical signal.
$L_{\max}$ maximum degree of expansion of geophysical signal.
l degree of spherical harmonic.
m order of spherical harmonic.
N spherical Shannon number.
n number of observations compared in misfit calculation.
p pressure.
p' dimensionless pressure.
R spatial region of interest.
s scalar geophysical function on the unit sphere.
s_{lm} spherical harmonic coefficients of the function s.
s_α Slepian basis coefficients of the function s.
u horizontal component of velocity.
$\mathbf{v}$ velocity vector.
x horizontal coordinate.
x' dimensionless horizontal coordinate.
Y_{lm} spherical harmonic on the unit sphere.
z vertical coordinate.
η viscosity (Newtonian).
η_{UM} viscosity of the upper mantle.
η_{TZ} viscosity of the transition zone.
η_{LM} viscosity of the lower mantle.
γ ratio of viscosities between mantle layers.
λ Slepian eigenvalues, or the fraction of signal energy concentrated locally.
Ω unit sphere.
ϕ longitude.
τ shear stress.
Θ colatitudinal radius of the region of interest.
θ_0 colatitude.

Acknowledgments

[63] This research was supported by the David and Lucile Packard Foundation and the National Science Foundation. We thank Nan Zhang for providing the data presented in Figures 5c and 5d. Helpful reviews by Clint Conrad and Scott King improved the clarity and quality of this work. Figures 1–7 were created with the GMT software [*Wessel and Smith*, 1998]. The Slepian analysis routines are available at http://www.frederik.net.

References

Artemieva, I. M. (2009), The continental lithosphere: Reconciling thermal, seismic, and petrologic data, *Lithos*, *109*, 23–46, doi:10.1016/j.lithos.2008.09.015.

Ballard, S., and H. N. Pollack (1987), Diversion of heat by Archean cratons: A model for southern Africa, *Earth Planet. Sci. Lett.*, *85*, 253–264.

Becker, T. W. (2006), On the effect of temperature and strain-rate dependent viscosity on global mantle flow, net rotation, and plate-driving forces, *Geophys. J. Int.*, *167*, 943–957, doi:10.1111/j.1365-246X.2006.03172.x.

Becker, T. W. (2008), Azimuthal seismic anisotropy constrains net rotation of the lithosphere, *Geophys. Res. Lett.*, *35*, L05303, doi:10.1029/2007GL032928.

Becker, T. W., J. B. Kellogg, G. Ekström, and R. J. O'Connell (2003), Comparison of azimuthal seismic anisotropy from surface waves and finite strain from global mantle-circulation models, *Geophys. J. Int.*, *155*, 696–714.

Becker, T. W., S. Chevrot, V. Schulte-Pelkum, and D. K. Blackman (2006), Statistical properties of seismic anisotropy predicted by upper mantle geodynamic models, *J. Geophys. Res.*, *111*, B08309, doi:10.1029/2005JB004095.

Behn, M. D., C. P. Conrad, and P. G. Silver (2004), Detection of upper mantle flow associated with the African Superplume, *Earth Planet. Sci. Lett.*, *224*, 259–274.

Cathles, L. M. (1975), *The Viscosity of the Earth's Mantle*, Princeton Univ. Press, Princeton, N. J.

Conrad, C. P., and M. D. Behn (2010), Constraints on lithosphere net rotation and asthenospheric viscosity from global mantle flow models and seismic anisotropy, *Geochem. Geophys. Geosyst.*, *11*, Q05W05, doi:10.1029/2009GC002970.

Conrad, C. P., and C. Lithgow-Bertelloni (2006), Influence of continental roots and asthenosphere on plate-mantle coupling, *Geophys. Res. Lett.*, *33*, L05312, doi:10.1029/2005GL025621.

Conrad, C. P., M. D. Behn, and P. G. Silver (2007), Global mantle flow and the development of seismic anisotropy: Differences between the oceanic and continental upper mantle, *J. Geophys. Res.*, *112*, B07317, doi:10.1029/2006JB004608.

Conrad, C. P., B. Wu, E. I. Smith, T. A. Bianco, and A. Tibbetts (2010), Shear-driven upwelling induced by lateral viscosity variations and asthenospheric shear: A mechanism for intraplate volcanism, *Phys. Earth Planet. Inter.*, *178*, 162–175, doi:10.1016/j.pepi.2009.10.001.

Debayle, E. (1999), SV-wave azimuthal anisotropy in the Australian upper mantle: Preliminary results from automated Rayleigh waveform inversion, *Geophys. J. Int.*, *137*, 747–754.

Debayle, E., and B. L. N. Kennett (2000a), The Australian continental upper mantle: Structure and deformation inferred from surface waves, *J. Geophys. Res.*, *105*, 25,423–25,450.

Debayle, E., and B. L. N. Kennett (2000b), Anisotropy in the Australian upper mantle from Love and Rayleigh waveform inversion, *Earth Planet. Sci. Lett.*, *184*, 339–351.

Debayle, E., B. L. N. Kennett, and K. Priestley (2005), Global azimuthal seismic anisotropy and the unique plate-motion deformation of Australia, *Nature*, *433*, 509–512.

Ekström, G., and A. M. Dziewoński (1998), The unique anisotropy of the Pacific upper mantle, *Nature*, *394*, 168–172.

Forsyth, D. W. (1975), The early structural evolution and anisotropy of the oceanic upper mantle, *Geophys. J. R. Astron. Soc.*, *43*, 103–162.

Forte, A. M., and W. R. Peltier (1994), The kinematics and dynamics of poloidal-toroidal coupling of mantle flow: The importance of surface plates and lateral viscosity variations, *Adv. Geophys.*, *36*, 1–119.

Fouch, M. J., and S. Rondenay (2006), Seismic anisotropy beneath stable continental interiors, *Phys. Earth Planet. Inter.*, *158*, 292–320.

Fouch, M. J., K. M. Fischer, E. M. Parmentier, M. E. Wysession, and T. J. Clarke (2000), Shear wave splitting, continental keels, and patterns of mantle flow, *J. Geophys. Res.*, *105*(B3), 6255–6275.

Freeden, W., and V. Michel (1999), Constructive approximation and numerical methods in geodetic research today—An attempt at a categorization based on an uncertainty principle, *J. Geod.*, *73*, 452–465.

Gilbert, H. J., A. F. Sheehan, D. A. Wiens, K. G. Dueker, L. M. Dorman, J. Hildebrand, and S. Webb (2001), Upper mantle discontinuity structure in the region of the Tonga Subduction Zone, *Geophys. Res. Lett.*, *28*(9), 1855–1858.

Gripp, A. E., and R. G. Gordon (2002), Young tracks of hotspots and current plate velocities, *Geophys. J. Int.*, *150*, 321–361.

Gung, Y., M. Panning, and B. Romanowicz (2003), Global anisotropy and the thickness of continents, *Nature*, *422*, 707–711.

Hager, B. H. (1984), Subducted slabs and the geoid: Constraints on mantle rheology and flow, *J. Geophys. Res.*, *89*(B7), 6003–6015.

Hager, B. H., and M. A. Richards (1989), Long-wavelength variations in Earth's geoid: Physical models and dynamical implications, *Philos. Trans. R. Soc. London*, *328*, 309–327.

Han, D., and J. Wahr (1995), The viscoelastic relaxation of a realistically stratified Earth, and a further analysis of postglacial rebound, *Geophys. J. Int.*, *120*(2), 287–311, doi:10.1111/j.1365-246X.1995.tb01819.x.

Han, L., and M. Gurnis (1999), How valid are dynamic models of subduction and convection when plate motions are prescribed?, *Phys. Earth Planet. Inter.*, *110*, 235–246.

Haxby, W. F., and D. L. Turcotte (1978), On isostatic geoid anomalies, *J. Geophys. Res.*, *83*(B11), 5473–5478.

Hess, H. H. (1964), Seismic anisotropy of the uppermost mantle under oceans, *Nature*, *203*, 629–631.

Hirth, G., R. L. Evans, and A. D. Chave (2000), Comparison of continental and oceanic mantle electrical conductivity: Is the Archean lithosphere dry?, *Geochem. Geophys. Geosyst.*, *1*(12), 1030, doi:10.1029/2000GC000048.

Jaupart, C., J. C. Mareschal, L. Guillou-Frottier, and A. Davaille (1998), Heat flow and thickness of the lithosphere in the Canadian Shield, *J. Geophys. Res.*, *103*(B7), 15,269–15,286.

Jung, H., and S. Karato (2001), Water-induced fabric transitions in olivine, *Science*, *293*, 1460–1463.

Kaminski, E., and N. M. Ribe (2001), A kinematic model for the recrystallization and texture development in olivine polycrystals, *Earth Planet. Sci. Lett.*, *189*, 253–267.

Karato, S., and P. Wu (1993), Rheology of the upper mantle: A synthesis, *Science*, *260*, 771–778.

Kennett, B. L. N., E. R. Engdahl, and R. Buland (1995), Constraints on seismic velocities in the Earth from travel times, *Geophys. J. Int.*, *122*, 108–124.

King, S. D. (2005), Archean cratons and mantle dynamics, *Earth Planet. Sci. Lett.*, *234*, 1–14, doi:10.1016/j.epsl.2005.03.007.

King, S. D., and G. Masters (1992), An inversion for radial viscosity structure using seismic tomography, *Geophys. Res. Lett.*, *19*(15), 1551–1554.

King, S. D., and J. Ritsema (2000), African hotspot volcanism: Small-scale convection in the upper mantle beneath cratons, *Science*, *290*, 1137–1140.

Lambeck, K., P. Johnston, and M. Nakada (1990), Holocene glacial rebound and sea-level change in NW Europe, *Geophys. J. Int.*, *103*(2), 451–468, doi:10.1111/j.1365-246X.1990.tb01784.x.

Lemoine, F. G., et al. (1998), The development of the joint NASA GSFC and NIMA geopotential model EGM96, *Tech. Rep. NASA/TP-1998-206861*, NASA Goddard Space Flight Cent., Greenbelt, Md.

Long, M. D., and P. G. Silver (2009), Shear wave splitting and mantle anisotropy: Measurements, interpretations, and new directions, *Surv. Geophys.*, *30*, 407–461, doi:10.1007/s10712-009-9075-1.

Marone, F., and B. Romanowicz (2007), The depth distribution of azimuthal anisotropy in the continental upper mantle, *Nature*, *447*, 198–201.

Masters, G., S. Johnson, G. Laske, H. Bolton, and J. H. Davies (1996), A shear-velocity model of the mantle, *Philos. Trans. R. Soc. London*, *354*, 1385–1411, doi:10.1098/rsta.1996.0054.

McAdoo, D. C. (1981), Geoid anomalies in the vicinity of subduction zones, *J. Geophys. Res.*, *86*(B7), 6073–6090.

McKenzie, D. (1979), Finite deformation during fluid flow, *Geophys. J. R. Astron. Soc.*, *58*, 689–715.

Mégnin, C., and B. Romanowicz (2000), The three-dimensional shear velocity structure of the mantle from the inversion of body, surface and higher-mode waveforms, *Geophys. J. Int.*, *143*, 709–728.

Mitrovica, J. X. (1996), Haskell [1935] revisited, *J. Geophys. Res.*, *101*(B1), 555–569.

Mitrovica, J. X., and A. M. Forte (2004), A new inference of mantle viscosity based upon joint inversion of convection and glacial isostatic adjustment data, *Earth Planet. Sci. Lett.*, *225*, 177–189, doi:10.1016/j.epsl.2004.06.005.

Mitrovica, J. X., K. Latychev, and M. E. Tamisiea (2007), Time variable gravity: Glacial isostatic adjustment, in *Treatise of Geophysics*, vol. 3, *Geodesy*, edited by T. Herring, pp. 197–211, doi:10.1016/B978-044452748-6.00175-9, Elsevier, Amsterdam.

Moresi, L., and M. Gurnis (1996), Constraints on the lateral strength of slabs from three-dimensional dynamic flow models, *Earth Planet. Sci. Lett.*, *138*, 15–28.

Müller, R. D., M. Sdrolias, C. Gaina, B. Steinberger, and C. Heine (2008), Long-term sea-level fluctuations driven by ocean basin dynamics, *Science*, *319*, 1357–1362.

Nakada, M., and K. Lambeck (1989), Late Pleistocene and Holocene sea-level change in the Australian region and mantle rheology, *Geophys. J. Int.*, *96*, 497–517.

Nyblade, A. A., and H. N. Pollack (1993), A global analysis of heat flow from Precambrian terrains: Implications for the thermal structure of Archean and Proterozoic lithosphere, *J. Geophys. Res.*, *98*(B7), 12,207–12,218.

Paulson, A., S. Zhong, and J. Wahr (2007a), Inference of mantle viscosity from GRACE and relative sea level data, *Geophys. J. Int.*, *171*, 497–508, doi:10.1111/j.1365-246X.2007.03556.x.

Paulson, A., S. Zhong, and J. Wahr (2007b), Limitations on the inversion for mantle viscosity from postglacial rebound, *Geophys. J. Int.*, *168*, 1195–1209, doi:10.1111/j.1365-246X.2006.03222.x.

Peltier, W. R. (1976), Glacial-isostatic adjustment II. The inverse problem, *Geophys. J. R. Astron. Soc.*, *46*, 669–705.
Peltier, W. R. (1998), Postglacial variations in the level of the sea: Implications for climate dynamics and solid-earth geophysics, *Rev. Geophys.*, *36*(4), 603–689.
Ribe, N. M. (1989), Seismic anisotropy and mantle flow, *J. Geophys. Res.*, *94*, 4213–4223.
Ribe, N. M. (1992), On the relation between seismic anisotropy and finite strain, *J. Geophys. Res.*, *97*, 8737–8747.
Ricard, Y., L. Fleitout, and C. Froidevaux (1984), Geoid heights and lithospheric stresses for a dynamical Earth, *Ann. Geophys.*, *2*, 267–286.
Ricard, Y., C. Froidevaux, and L. Fleitout (1988), Global plate motion and the geoid: A physical model, *Geophys. J. Int.*, *93*, 477–484.
Ricard, Y., M. Richards, C. Lithgow-Bertelloni, and Y. L. Stunff (1993), A geodynamic model of mantle density heterogeneity, *J. Geophys. Res.*, *98*(B12), 21,895–21,909.
Ritsema, J., H. J. van Heijst, and J. H. Woodhouse (2004), Global transition zone tomography, *J. Geophys. Res.*, *109*, B02302, doi:10.1029/2003JB002610.
Rudnick, R. L., W. F. McDonough, and R. J. O'Connell (1998), Thermal structure, thickness and composition of continental lithosphere, *Chem. Geol.*, *145*, 395–411.
Savage, M. K. (1999), Seismic anisotropy and mantle deformation: What have we learned from shear wave splitting?, *Rev. Geophys.*, *37*, 65–106.
Shapiro, N. M., and M. H. Ritzwoller (2002), Monte-Carlo inversion for a global shear-velocity model of the crust and upper mantle, *Geophys. J. Int.*, *151*, 88–105.
Silver, P. G. (1996), Seismic anisotropy beneath the continents: Probing the depths of geology, *Annu. Rev. Earth Planet. Sci.*, *24*, 385–432.
Silver, P. G., S. S. Gao, K. H. Liu, and the Kaapvaal Seismic Group (2001), Mantle deformation beneath southern Africa, *Geophys. Res. Lett.*, *28*, 2493–2496.
Simons, F. J., and F. A. Dahlen (2006), Spherical Slepian functions and the polar gap in geodesy, *Geophys. J. Int.*, *166*, 1039–1061, doi:10.1111/j.1365-246X.2006.03065.x.
Simons, F. J., and R. D. van der Hilst (2002), Age-dependent seismic thickness and mechanical strength of the Australian lithosphere, *Geophys. Res. Lett.*, *29*(11), 1529, doi:10.1029/2002GL014962.
Simons, F. J., and R. D. van der Hilst (2003), Seismic and mechanical anisotropy and the past and present deformation of the Australian lithosphere, *Earth Planet. Sci. Lett.*, *211*, 271–286, doi:10.1016/S0012-821X(03)00198-5.
Simons, F. J., R. D. van der Hilst, J.-P. Montagner, and A. Zielhuis (2002), Multimode Rayleigh wave inversion for heterogeneity and azimuthal anisotropy of the Australian upper mantle, *Geophys. J. Int.*, *151*(3), 738–754, doi:10.1046/j.1365-246X.2002.01787.x.
Simons, F. J., R. D. van der Hilst, and M. T. Zuber (2003), Spatiospectral localization of isostatic coherence anisotropy in Australia and its relation to seismic anisotropy: Implications for lithospheric deformation, *J. Geophys. Res.*, *108*(B5), 2250, doi:10.1029/2001JB000704.
Simons, F. J., F. A. Dahlen, and M. A. Wieczorek (2006), Spatiospectral concentration on a sphere, *SIAM Rev.*, *48*(3), 504–536, doi:10.1137/S0036144504445765.
Simons, F. J., J. C. Hawthorne, and C. D. Beggan (2009), Efficient analysis and representation of geophysical processes using localized spherical basis functions, *Proc. SPIE Int. Soc. Opt. Eng.*, *7446*, 74460G, doi:10.1117/12.825730.
Simons, M., and B. H. Hager (1997), Localization of the gravity field and the signature of glacial rebound, *Nature*, *390*, 500–504.
Tamisiea, M. E., J. X. Mitrovica, and J. L. Davis (2007), GRACE gravity data constrain ancient ice geometries and continental dynamics over Laurentia, *Science*, *316*, 881–883, doi:10.1126/science.1137157.
Turcotte, D. L., and E. R. Oxburgh (1967), Finite amplitude convection cells and continental drift, *J. Fluid Mech.*, *28*, 29–42.
Turcotte, D. L., and G. Schubert (2002), *Geodynamics*, 2nd ed., Cambridge Univ. Press, Cambridge, U. K.
van Hunen, J., S. Zhong, N. M. Shapiro, and M. H. Ritzwoller (2005), New evidence for dislocation creep from 3-D geodynamic modeling of the Pacific upper mantle structure, *Earth Planet. Sci. Lett.*, *238*, 146–155, doi:10.1016/j.epsl.2005.07.006.
Verma, R. K. (1960), Elasticity of some high-density crystals, *J. Geophys. Res.*, *65*, 757–766.
Walker, K. T., G. H. R. Bokelmann, S. L. Klemperer, and A. A. Nyblade (2005), Shear-wave splitting around hotspots: Evidence for upwelling-related mantle flow?, *Spec. Pap. Geol. Soc. Am.*, *388*, 171–192.
Wessel, P., and W. H. F. Smith (1998), New, improved version of Generic Mapping Tools released, *Eos Trans. AGU*, *79*(47), 579.
Wieczorek, M. A., and F. J. Simons (2005), Localized spectral analysis on the sphere, *Geophys. J. Int.*, *162*, 655–675, doi:10.1111/j.1365-246X.2005.02687.x.
Wu, P., and W. R. Peltier (1982), Viscous gravitational relaxation, *Geophys. J. R. Astron. Soc.*, *70*(2), 435–485.
Wu, P., and W. R. Peltier (1983), Glacial isostatic adjustment and the free air gravity anomaly as a constraint on deep mantle viscosity, *Geophys. J. R. Astron. Soc.*, *74*, 377–450.
Yuen, D. A., and R. Sabadini (1985), Viscosity stratification of the lower mantle as inferred from the J2 observation, *Ann. Geophys.*, *3*, 647–654.
Zhang, N., S. Zhong, W. Leng, and Z.-X. Li (2010), A model for the evolution of the Earth's mantle structure since the early Paleozoic, *J. Geophys. Res.*, doi:10.1029/2009JB006896, in press.
Zhang, S., and S. Karato (1995), Lattice preferred orientation of olivine aggregates deformed in simple shear, *Nature*, *375*, 774–777.
Zhong, S. (2001), Role of ocean-continent contrast and continental keels on plate motion, net rotation of lithosphere, and the geoid, *J. Geophys. Res.*, *106*(B1), 703–712.
Zhong, S. (2006), Constraints on thermochemical convection of the mantle from plume heat flux, plume excess temperature, and upper mantle temperature, *J. Geophys. Res.*, *111*, B04409, doi:10.1029/2005JB003972.